INSTITUTE OF PHYSICS PUBLISHING MODELLING AND SIMULATION IN MATERIALS SCIENCE AND ENGINEERING

Modelling Simul. Mater. Sci. Eng. **11** (2003) 265–286 PII: S0965-0393(03)53075-3

A multiscale analysis of fixed-end simple shear using molecular dynamics, crystal plasticity, and a macroscopic internal state variable theory

M F Horstemeyer[1], M I Baskes[2], V C Prantil[3], J Philliber[4] and S Vonderheide[4]

[1] Mechanical Engineering Department, Mississippi State University, 206 Carpenter Bldg, Mississippi State, MS 39762, USA
[2] MST-8, MS G755, Los Alamos National Laboratory, Los Alamos, NM 87545, USA
[3] Milwaukee School of Engineering, Mech. Engr. Dept, S229, Milwaukee, WI53202-3109, USA
[4]Center for Materials and Engineering Sciences, Sandia National Laboratories, Livermore, CA 94551-0969, USA

Received 10 March 2002, 4 August 2002
Published 24 February 2003
Online at stacks.iop.org/MSMSE/11/265

Abstract

We examine FCC nickel undergoing simple shear by using three different numerical frameworks formulated at three different size scales. The three frameworks included embedded atom method potentials used in molecular dynamics simulations, crystal plasticity used in finite element simulations, and a macroscale internal state variable formulation used in finite element simulations. Simple shear simulations were performed in which the specimen aspect ratio was varied to give insight into the homogeneous and inhomogeneous aspects of large deformation. This study revealed that the 'apparent' yield stress was sensitive to the specimen aspect ratio except when the length-to-height ratio reached about 8 : 1, the yield stress remained constant. The three numerical frameworks gave similar qualitative responses related to inhomogeneous stress and strain distributions in the corner regions of the specimens and also similar responses in the centralized homogeneous deformation region. However, when comparing the shear stress distribution for the finite element analyses to the atomistic simulations, a much narrower distribution arose for the finite element analyses due to the lack of thermal vibrations experienced in the atomistic simulations at 300 K. A 10 K an atomistic simulation which dampened out the high frequency thermal vibrations verified this reasoning. Three different sizes of blocks of atoms were also used in the atomistic simulations and the results showed very similar stress and strain distributions with respect to each other indicating that no size scale effect is evidenced when normalized by the global shear stress. However, a size scale effect exists related to the global (volume average) shear stress in the specimen. As the specimen size increased, the yield stress decreased. Finally, when comparing the three different numerical frameworks, the location of maximum dislocation nucleation occurred at the location of the maximum plastic spin, stress gradients, and strain gradients.

1. Introduction

In this study, we explore three different numerical modelling frameworks for evaluating plasticity in simple shear of nickel. The numerical frameworks include atomistic modelling, crystal plasticity using finite elements, and internal state variable theory using finite elements. Starting from the atomistic to the crystal plasticity and then to the macroscale internal state variable frameworks, the degrees of freedom in the simulations decrease. The atomistic simulations start from one atom and build up. The crystal plasticity formulation starts at the scale of the grain and builds up. And the macroscale internal state variable starts from a macroscale continuum point, which usually represents a polycrystalline material. As such, the macroscale internal state variable formulation does not include explicit details about the plastic spin (texture effect) nor the atomic level dislocations, but the crystal plasticity and atomistic formulations do. Furthermore, the macroscale internal state variable theory and crystal plasticity formulations do not include the thermal velocity (and vibration) effects related to atomic rearrangement or subgrain division arising from large strains, but the atomistic formulation does.

In order to bridge length scales, one can perform physical experiments to quantify the appropriate cause–effect relations between the microstructure and mechanical properties. However, these experiments are costly and to date are wanting. An alternative view is to use 'numerical' experiments by using different numerical methods that clearly describe the cause–effect relations at different size scales. As a side note, we are not claiming that the crystal plasticity nor the internal state variable models have an explicit length scale parameter (they are size independent), but because of their kinematic starting points represent different scales. Because the crystal plasticity kinematics starts at the level of the crystal, rotations, strains, and hence stresses would be different than the macroscale internal state variable formulation. One might argue that the crystal plasticity and macroscale internal state variable formulations really represent the same scale because the hardening equations could be intermixed in the formulations, and no inherent length scale parameters exist. However, because of kinematic rotations, the specimen stresses of the crystal plasticity and macroscale internal state variable formulations would be very different. By comparing then the macroscale internal state and the crystal plasticity formulations with the atomistic simulations, we can clearly distinguish the role of the kinematics. Before this writing, neither multiscale physical experiments nor multiscale numerical experiments have been performed on a material like single crystal nickel; hence, this is our contribution.

Researchers have investigated the response of constitutive models to simple shear or torsion for years, because crystallographic slip occurs on shear planes. In this study, we do not strictly examine simple shear. Simple shear requires that the face of the continuum point remain planar and parallel, strictly speaking. We loosen the planar and parallel requirement to analyse the inhomogeneous and homogeneous portions of the material block for the modelling frameworks. Our ultimate goal was to examine general shearing experiments, which do not constrain the traction free faces to be planar and parallel and as such our boundary conditions are more applicable to shear experiments.

The paper is outlined as follows. Section 2 briefly describes the three modelling frameworks. Section 3 presents the results and a discussion focused on comparing and contrasting the results, and some conclusions are presented in section 4.

2. Simulation preliminaries

In this section, we briefly describe the pertinent attributes of the three numerical methods related to plasticity at different length scales for nickel. The atomistic simulations were conducted

using embedded atom method (EAM) potentials (Daw and Baskes 1984). Finite element simulations using ABAQUS were conducted using two different constitutive models. One model was a crystal plasticity formulation based on the Cuitino and Ortiz (1992) kinematics first proposed by Hill and Rice (1972) but with the hardening equations from Horstemeyer *et al* (1999). Another constitutive model used was a macroscale internal state variable theory from the work of Bammann (1990), Bammann *et al* (1993, 1996).

For the boundary conditions in all three cases, we apply a velocity at the top of the material in a horizontal, shearing manner and fix the nodes or atoms at the bottom. We keep the left and right sides free from tractions. Also keep in mind that the atomistic simulations are of the nanometre scale, and the continuum simulations are of the centimetre scale. We mention this only to give the reader an idea of the orders of magnitude difference in the simulations. The size scales are represented by the context of the models not the geometry of the meshes. We discuss mesh issues in the section when we discuss specimen aspect ratios.

2.1. Atomistic simulation background

The atomistic simulations employed embedded atom potentials developed by Daw and Baskes (1984) proposed as a numerical method for calculating atomic energetics of metals. Daw *et al* (1993) review several applications of EAM. Essentially, EAM comprises a cohesive energy of an atom determined by the local electron density into which that atom is placed. A function, ρ, is viewed as the contribution to the electron density at a site due to the neighbouring atoms. The embedding energy F^i is associated with placing an atom in that electron environment. The functional form of the total energy is given by

$$E = \sum_i F^i \left(\sum_{i \neq j} \rho^i \left(r^{ij} \right) \right) + \frac{1}{2} \sum_{ij} \phi^{ij} \left(r^{ij} \right), \tag{1}$$

where i refers to the atom in question and j refers to the neighbouring atom, r^{ij} is the separation distance between atoms i and j, and ϕ^{ij} is the pair potential. Subscripts denote the rank of the tensor, for example, one subscript denotes a vector, two subscripts denote a second rank tensor, and so on. Superscripts identify the atom of interest. In molecular dynamics, the energy is used to determine the forces on each atom,

$$f_k^{ij} = \sum_{j(\neq i)}^{N} \frac{\partial E}{\partial r^{ij}} \frac{r^{ij}}{|r^{ij}|}. \tag{2}$$

At each atom the dipole force tensor, $\underline{\beta}$ (termed as the local stress tensor hereafter) is given by

$$\beta_{km}^i = \frac{1}{\Omega^i} \sum_{j(\neq i)}^{N} f_k^{ij} r_m^{ij}, \tag{3}$$

where i refers to the atom in question and j refers to the neighbouring atom, f_k^{ij} is the force vector between atoms, r_m^{ij} is a position vector between atoms i and j, N is the number of nearest neighbour atoms, and Ω^i is the atomic volume. When stress is defined at an atom, then β_{km}^i is the stress tensor at that point. Since stress is defined at a continuum point, we determine the stress tensor (termed the global continuum stress hereafter) as a volume average over the specimen,

$$\sigma_{mk} = \frac{1}{N^*} \sum_{i}^{N^*} \beta_{mk}^i, \tag{4}$$

in which the stress tensor is defined in terms of the total number of active atoms, N^*, in the specimen. We took this averaged stress then to determine the stress–strain response and yield point of the specimen.

The EAM potential for nickel was developed by Angelo *et al* (1995) with a lattice parameter of 3.52 Å. The EAM potential was implemented into a molecular dynamics framework.

2.2. Crystal plasticity background

For the single crystal kinematics, the multiplicative decomposition of the deformation gradient into elastic (including rigid lattice rotation) and plastic parts is assumed, i.e. $\underline{F} = \underline{F}^{\mathrm{e}}\underline{F}^{\mathrm{p}} \cdot \underline{F}^{\mathrm{p}}$ is computed at the end of the time step by applying the following:

$$\underline{F}^{\mathrm{p}}_{t+\Delta t} = \exp(\underline{L}^{\mathrm{p}}\Delta t)\underline{F}^{\mathrm{p}}_{t}, \tag{5}$$

where $\underline{F}^{\mathrm{p}}_{t}$ and $\underline{F}^{\mathrm{p}}_{t+\Delta t}$ are the plastic deformation gradients at the beginning and end of the time step, respectively. $\underline{L}^{\mathrm{p}}$ is the plastic velocity gradient in the intermediate configuration that occurs during the time step, which is determined by (Asaro 1983)

$$\underline{L}^{\mathrm{p}} = \sum_{i=1}^{N} \dot{\gamma}_i (\underline{s}_i \otimes \underline{m}_i), \tag{6}$$

where N is the number of slip systems, $\dot{\gamma}_i$ is the continuum slip or shear rate on the ith slip system, $\underline{s}_i$ is the slip direction vector, and $\underline{m}_i$ is the slip plane normal vector. The hyperelastic stress–strain relation is specified in the intermediate, or stress-free, configuration as

$$\underline{\sigma}(\underline{\hat{E}}) = \underline{C} : \underline{\hat{E}}, \tag{7}$$

where the elastic stiffness tensor, $\underline{C}$, is objective for a given crystal in the intermediate configuration (cf Asaro (1983)). The intermediate configuration is aligned with the crystalline axes. $\underline{\hat{\sigma}}$ is the second Piola–Kirchhoff stress in the intermediate configuration, and $\underline{\hat{E}}$ is the conjugate Green elastic strain.

The viscoplastic kinetic relation used is a kinematic hardening generalization of the form employed by Hutchinson (1976), i.e.

$$\dot{\gamma}_i = \dot{\gamma}_0 \operatorname{sgn}(\tau_i - \alpha_i)\left|\frac{\tau_i - \alpha_i}{g_i}\right|^M, \tag{8}$$

where the plastic slip rate on the ith slip system, $\dot{\gamma}_i$, is a function of a fixed reference strain rate, $\dot{\gamma}_0$, the reference shear strength, g_i, the resolved shear stress on the slip system, τ_i, the rate sensitivity exponent for the material, M, and an internal state variable representing kinematic hardening effects resulting from backstress at the slip system level, α_i. The isotropic hardening evolution law for the internal hardening state variable, g_i, on ith slip system is given by

$$\dot{g}_i = \sum_{i,j=1}^{12} h_{ij}\dot{\gamma}_j, \tag{9}$$

where h_{ij} are the hardening (or plastic) moduli. The self-hardening components arise when $i = j$ and the latent hardening components arise when $i \neq j$. The increase or decrease of flow stress on a secondary slip system due to crystallographic slip on an active slip system is referred to as latent hardening. A modified hardening-recovery equation was used with the PAN rule (Peirce *et al* 1982) given by

$$h_{ij} = Z(\gamma)(\delta_{ij} + \mathrm{lhr}(1 - \delta_{ij})), \tag{10}$$

where lhr is the latent hardening ratio. The modified Armstrong and Frederick (1966) hardening-recovery equation that was also used is given by

$$Z(\gamma) = h_0 - Rg(\gamma), \tag{11}$$

where R is a material constant. We employ a substructural internal variable evolution equation (Horstemeyer and McDowell, 1998) that is assumed to evolve at the level of the grain. For the Armstrong–Frederick form, we employ the following form for each crystal

$$\dot{\alpha}_i = C_{\text{rate}}(C_{\text{sat}}\dot{\gamma}_i - \alpha_i \|\dot{\gamma}_i\|), \tag{12}$$

where C_{rate} controls the rate of evolution, and C_{sat} is the saturation level of the backstress. These two parameters were chosen to fit the experimental data. The substructural hardening internal state variable reflects dislocation interactions within the grain (cf Rice (1971)) and follows the Coleman and Gurtin (1967) postulate that the rate must be governed by a differential equation in which the plastic rate of deformation appears.

Once the material constants were determined from single crystal nickel experiments (Edington 1969), simple shear simulations were run with different geometries, and the volume average of the shear stress was used for the discussion purposes to follow. We should note here that although yield is included in the formulation, there exists an 'apparent' yield for the specimen when all of the element stresses are averaged. In the discussion section, we use the word 'yield' in the sense of the apparent yield stress to make comparisons with the atomistic simulations.

2.3. Macroscale internal state variable theory background

For the internal state variable (ISV) plasticity model (Bammann 1990, Bammann *et al* 1993, 1996) used in this study, the kinematics and work hardening equations are similar to the crystal plasticity formulation except that the intermediate configuration is not aligned necessarily to the crystalline axis of a single crystal due to the absence of a plastic spin component. The pertinent equations in this model are denoted by the rate of change of the observable and internal state variables. The equations used within the context of the finite element method are given by,

$$\overset{o}{\underline{\sigma}} = \underline{\dot{\sigma}} - \underline{W}^{\text{e}}\underline{\sigma} - \underline{\sigma}\,\underline{W}^{\text{e}} = \lambda tr(\underline{D}^{\text{e}})\underline{I} + 2\mu\underline{D}^{\text{e}}, \tag{13}$$

$$\underline{D}^{\text{e}} = \underline{D} - \underline{D}^{\text{in}}, \tag{14}$$

$$\underline{D}^{\text{in}} = f(t)\sinh\left\lfloor \frac{\|\underline{\sigma}' - \underline{\dot{\alpha}}\| - \{R + Y(T)\}}{V(T)} \right\rfloor \frac{\underline{\sigma}' - \underline{\alpha}}{\|\underline{\sigma}' - \underline{\alpha}\|}, \tag{15}$$

$$\overset{o}{\underline{\alpha}} = \underline{\dot{\alpha}} - \underline{W}^{\text{e}}\underline{\alpha} + \underline{\alpha}\underline{W}^{\text{e}} = \left\{ h(T)\underline{D}^{\text{in}} - \left\lfloor \sqrt{\frac{2}{3}} r_{\text{d}}(T)\|\underline{D}^{\text{in}}\| + r_{\text{s}}(T) \right\rfloor \|\underline{\alpha}\|\underline{\alpha} \right\}, \tag{16}$$

$$\dot{R} = \left\{ H(T)\underline{D}^{\text{in}} - \left\lfloor \sqrt{\frac{2}{3}} R_{\text{d}}(T)\|\underline{D}^{\text{in}}\| + R_{\text{s}}(T) \right\rfloor R^2 \right\}. \tag{17}$$

The rate equations are generally written as objective rates ($\overset{o}{\underline{\sigma}}$, $\overset{o}{\underline{\alpha}}$) assuming a Jaumann rate in which the continuum spin equals the elastic spin ($\underline{W} = \underline{W}^{\text{e}}$). The internal state variable (ISV) equations (16) and (17) are functions of the observable variables (temperature, stress state, and rate of deformation). In general, the rate equations of generalized displacements, or thermodynamics fluxes, describing the rate of change may be written as independent equations for each ISV or as derivatives of a suitably chosen potential function arising from the hypothesis

of generalized normality (Rice 1971). In equation (13), the elastic polycrystalline Lame constants are denoted by λ and μ; hence, a slight difference existed in the elastic modulus for the single crystal plasticity formulation and the polycrystal ISV formulation. The elastic rate of deformation ($\underline{D}^{\mathrm{e}}$) results when the flow rule as shown in equation (15) is subtracted from the total deformation ($\underline{D}$), which is defined by the boundary conditions.

The independent variables for the inelastic rate of deformation are given in equation (14) as the stress, temperature, and internal state variables. The deviatoric inelastic flow rule, $\underline{D}^{\mathrm{in}}$, encompasses the regimes of creep and plasticity and is a function of the temperature, the kinematic hardening internal state variable ($\underline{\alpha}$), the isotropic hardening internal state variable (R), and the functions $f(T)$, $V(T)$, and $Y(T)$, which are related to yielding with Arrhenius-type temperature dependence. The function $Y(T)$ is the rate-independent yield stress. The function $f(T)$ determines when the rate-dependence affects initial yielding. The function $V(T)$ determines the magnitude of rate-dependence on yielding. These functions are determined from isothermal compression tests with different strain rates and temperatures,

$$V(T) = C_1 \exp\left(-\frac{C_2}{T}\right), \qquad Y(T) = C_3 \exp\left(\frac{C_4}{T}\right), \qquad f(T) = C_5 \exp\left(-\frac{C_6}{T}\right). \tag{18}$$

The kinematic hardening internal state variable, $\underline{\alpha}$, reflects the effect of anisotropic dislocation density, and the isotropic hardening internal state variable R, reflects the effect of the global dislocation density. The functions $r_{\mathrm{s}}(T)$ and $R_{\mathrm{s}}(T)$ are scalar in nature and describe the diffusion-controlled static or thermal recovery, while $r_{\mathrm{d}}(T)$ and $R_{\mathrm{d}}(T)$ are scalar functions describing dynamic recovery. Hence, the two main types of recovery that are exhibited by populations of dislocations within crystallographic materials are captured in the ISVs. Note that the discrete dislocations that are present in the EAM simulations are not explicitly included here. In the context of this paper, the static recovery terms are set to zero. The anisotropic hardening modulus is $h(T)$, and the isotropic hardening modulus is $H(T)$.

$$r_{\mathrm{d}}(T) = C_7 \exp\left(-\frac{C_8}{T}\right), \tag{19}$$

$$h(T) = C_9 - C_{10}T, \tag{20}$$

$$r_s(T) = C_{11} \exp\left(-\frac{C_{12}}{T}\right), \tag{21}$$

$$R_{\mathrm{d}}(T) = C_{13} \exp\left(-\frac{C_{14}}{T}\right), \tag{22}$$

$$H = C_{15} - C_{16}T, \tag{23}$$

$$R_s(T) = C_{17} \exp\left(-\frac{C_{18}}{T}\right). \tag{24}$$

The material constants were determined from the polycrystalline nickel experiments (Hughes and Nix 1988) used for the crystal plasticity formulation. Then simple shear simulations were run with different geometries, and the volume average of the shear stress in the elements was used. The same comments about the yield stress and apparent yield stress of the specimen is same as the crystal plasticity formulation to make comparisons with the atomistic simulations.

2.4. Computational setup

For all three numerical methods, fixed-end simple shear boundary conditions were prescribed in which the computational specimen had free surfaces in the x- and y-directions was periodic in the z-direction (see figure 1 for reference). The initial temperature was set at 300 K. The applied strain rate for the atomistic simulations was very large ($\sim 1 \times 10^9\ \mathrm{s}^{-1}$), while the parameters for the crystal plasticity and macroscale ISV models were determined from rate-independent rates ($\sim 1 \times 10^4\ \mathrm{s}^{-1}$). This introduces a contrast in stresses since the larger applied strain rate would induce a larger stress level. Hence, there exists not only a size scale difference but a timescale difference between the atomistic simulations and the continuum level simulations. For the EAM and crystal plasticity simulations, the crystal orientation was $[100, 011, 0\bar{1}1]$, and the loading on y-face was in the [100] direction. Another study (Horstemeyer *et al* 2002) focused on varying orientation effects showed that the atomistic methods provide the same general Schmid-type responses as macroscopic theories. For the macroscale ISV model, the crystallographic orientation cannot be represented discretely, although some deformation-induced anisotropy is included in the kinematic hardening variable.

In this study, we focused on fixed-end simple shear at the three size scales because we had planned a complementary experimental study that is yet to be completed with different size specimens in this condition. For the atomistic study, some other comments are warranted. In a previous atomistic study, Horstemeyer and Baskes (1999) showed that in fixed-end simulations, the global continuum stress saturates if the z-direction is four or more unit cells in thickness; smaller specimens introduce a separate size scale effect. Since a goal was to model the largest cross-sectional area possible, we used a four unit cell z-direction thickness in our simulations. After creating the samples with a desired crystal orientation, a few planes of atoms at the top and bottom (xz planes at the +y and −y extreme) were frozen on their perfect lattice sites. For initialization, the remainder of the atoms were allowed to energetically minimize their positions to accommodate any relaxation at the two remaining free surfaces (yz planes). Two types of velocities are considered in these simulations: the applied velocity and the thermal velocity from the atomic vibrations. Thermal velocities of the interior (or active, non-frozen atoms) were initialized at a chosen temperature (typically 300 K). For simple shear, a strain rate was then applied to the block of atoms by setting the x-velocity of the frozen xz planes to a constant value. The bottom atomic plane had a prescribed x-velocity of zero for the duration of the dynamics simulation, and the top atomic plane had a prescribed constant velocity to create a strained sample. If just the top row of atoms initially experienced the prescribed velocity without the active internal atoms experiencing the same velocity field, a shock was induced into the specimen because of the high strain rates. In our calculations, we introduced an initial applied velocity field that mitigated the shock wave and then applied the boundary velocity fields. To accomplish this, the interior atoms in the model were also given an initial x-velocity (superposed on their thermal 300 K velocities) that ramped linearly from 0.0 to the prescribed velocity at the top atomic plane depending on their y-coordinates in the simulation box.

One final notion regarding the yield point is worth mentioning and is illustrated by figure 1. We define two microyield points and a macroyield point to give understanding of yield for the atomistic simulations. First, the average global stress of the active atoms was computed in equation (3), and a stress–strain curve was plotted. We distinguish between three locations on the curve. The first location is defined as microyield 1, where the stress–strain behaviour first deviates from elastic linearity, i.e. the proportional limit. At this point, initial dislocations are emitted from the surface because of the local stress gradients near the corners. The second location is microyield 2, which is defined by the macroscale continuum concept of a 0.2% offset strain. The third location is defined as macroyield, the point at which the maximum

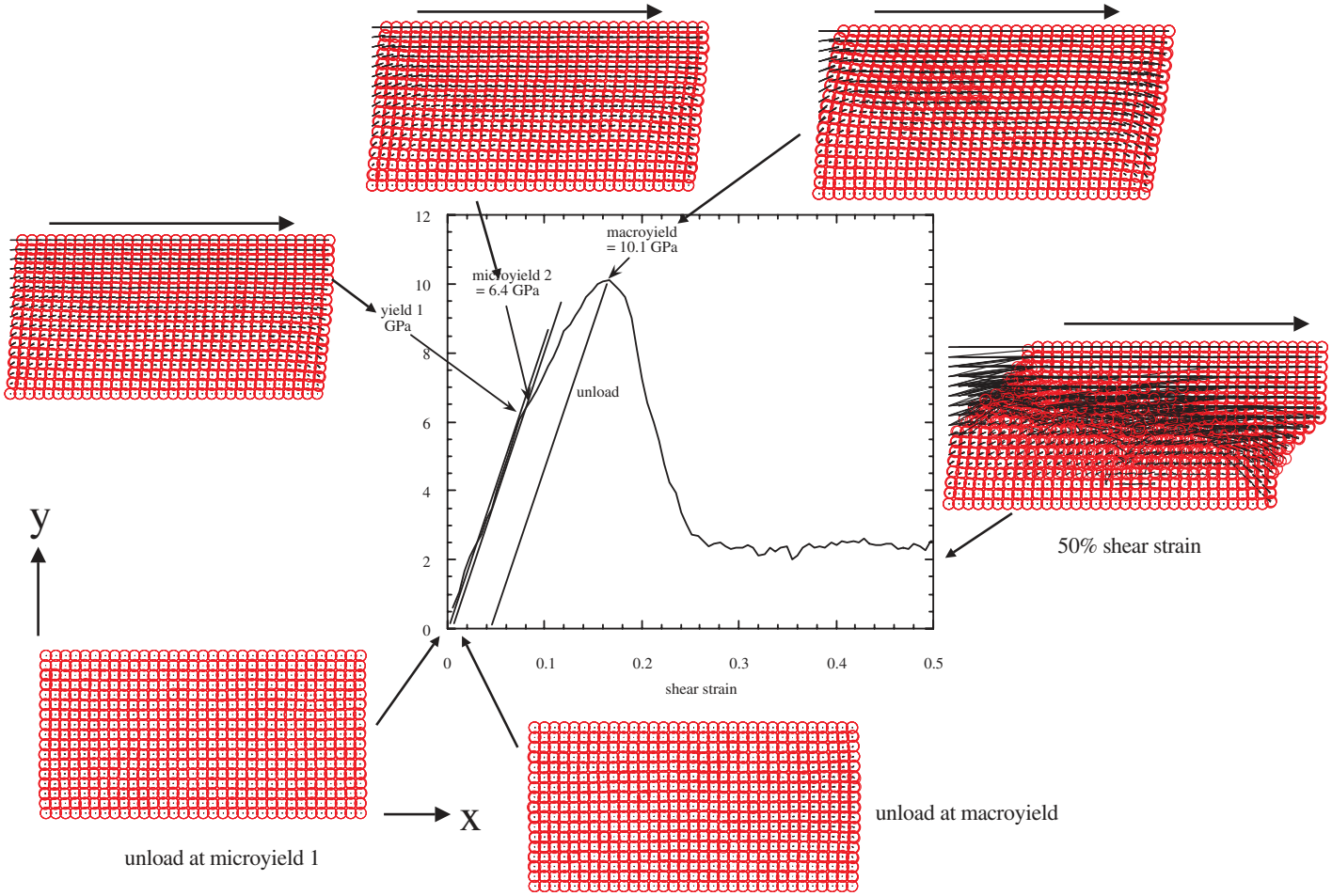

Figure 1. Shear stress–strain curve for 2242 atoms of nickel illustrating atomic positions and relative displacements (denoted by arrows on atoms) at different strain levels.

stress occurs. Because we start with perfect lattices, all initial defects are eliminated. As such the stress–strain responses, in terms of the stress drop-off, look very similar to experimental data of metal 'whiskers' which have essentially no initial defects (cf Yoshida *et al* (1966)). In whiskers, experiments have shown that yield is typically defined at the 'macroyield' point. At this point, the stress required to activate a certain density of dislocations is reached and the material plastically deforms precipitating dislocations with subsequent propagation of local Luders bands that lead to irregular fluctuations in the plateau region of the stress–strain curve after the macroyield stress drop-off. Figure 1 illustrates that microyield 1 and microyield 2 are essentially the same and in many cases, as exemplified in the ten thousand atom simulation, macroyield is very close to the other two microyield points.

In determining the yield points in many of the simulations, we also unloaded the material block at each of the microyield and macroyield points to give information regarding permanent set and the influence of dislocations on the yield points. In figure 1, we show the atom positions at different locations along a simple shear deformation path for a block of nickel material with 2242 atoms. Here, we unloaded at microyield 1 and microyield 2. It is clear from this simulation that the unload at microyield 1, returns the atoms to their original positions and at microyield 2 almost returns the atoms to their original positions with several dislocations remaining in the block near the right-hand edge of the block.

3. Results and discussion

In this section, we first discuss the qualitative comparisons of the results from the three types of simulations. Afterwards, we discuss the quantitative differences and describe the underlying mechanisms that are attributed to the aspect ratio of the specimen, material model, stress state, and kinetics.

First, in all of the atomistic simulations, dislocations nucleate from the free-surfaces of the x-faces and in particular, near the specimen corners where inhomogeneous deformation arises. Figure 2 illustrates this point for an eight-by-one x/y aspect ratio. Figure 2(a) shows a close-up view of the corner in which the dislocations were nucleated. Clearly, the shear stresses as designated by the brown colours are higher near the corner when contrasted with the bulk atomic shear stresses, which show an almost homogeneous distribution of yellow atoms in figure 2(b). Figure 2(c) shows that as deformation proceeds to 30% strain that the dislocations populate the whole material bulk.

To further illustrate the flow of dislocations, we employ the centrosymmetry parameter of Kelchner *et al* (1998), which shows deviations of the atomic positions from original lattice positions. Figure 3 shows colour contours of the centrosymmetry parameter at different strains in the stress–strain response. The second picture in figure 3 approximately corresponds to figures 2(a) and (b) year yield. Also, figure 2(c) corresponds to the last picture in figure 3 at 30% strain. When comparing figures 2 and 3, one can see that the stress response (figure 2) and centrosymmetry parameter (figure 3) correlate fairly well in signifying the dislocation nucleation, motion, and interaction.

Figures 4 and 5 compare the shear stress and shear strain responses, respectively, of the three numerical methods for the one-by-one specimen. Figures 6 and 7 show the same comparisons for the eight-by-one specimen. Interestingly, the material response at the corners due to these boundary conditions is the same for each numerical method whether you examine the stress or strain. Although the magnitude of the stress is different for each method (because of the size scale and applied strain rate), the kinematic response is essentially the same. This is extremely important for development of the kinematics of higher scale modelling such as a crystal plasticity model or a macroscale ISV model. One can also see that the centre region of

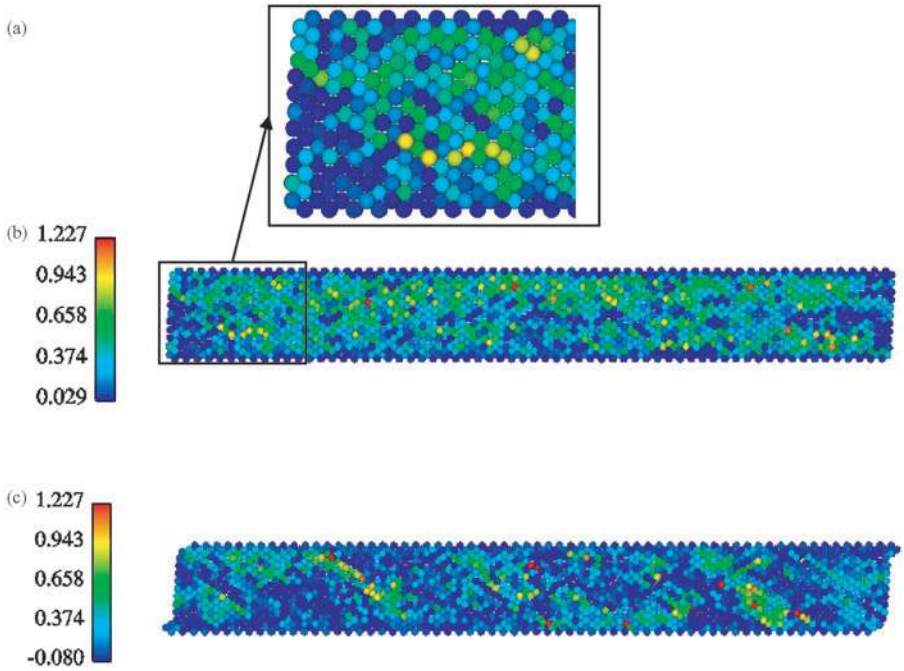

Figure 2. Shear stress contour plots (GPa) at (*a*) yield-zoom, (*b*) yield, and (*c*) 30% strain, illustrating the deformation response for a length-to-height ratio of approximately 8 : 1 (225 Å by 28 Å) simulation.

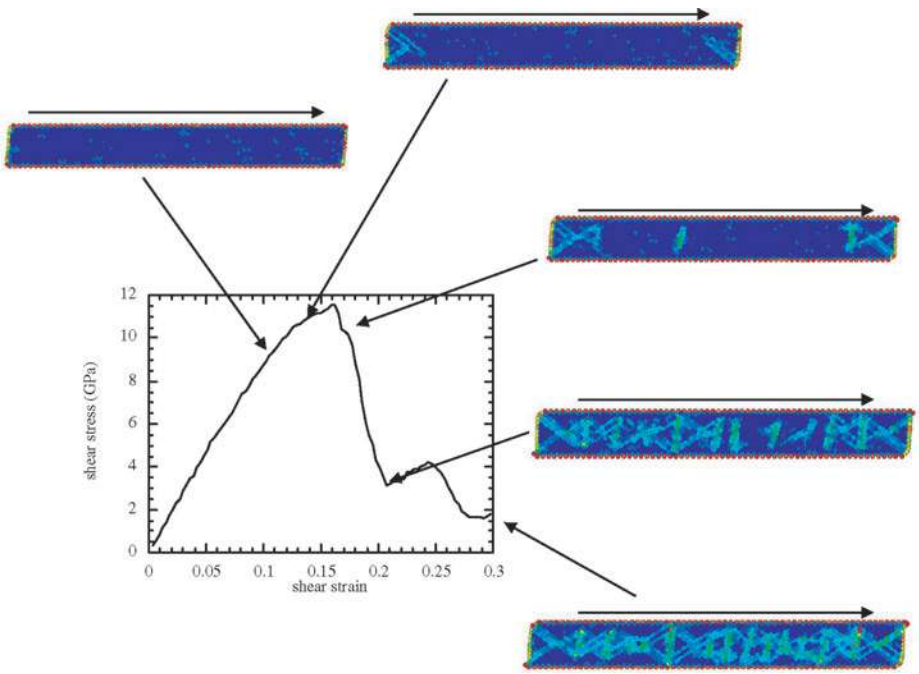

Figure 3. Average stress–strain response of an 8 : 1 specimen (225 Å by 28 Å) simulation with the centrosymmetry parameter illustrating the dislocation nucleation, motion, and interaction throughout deformation.

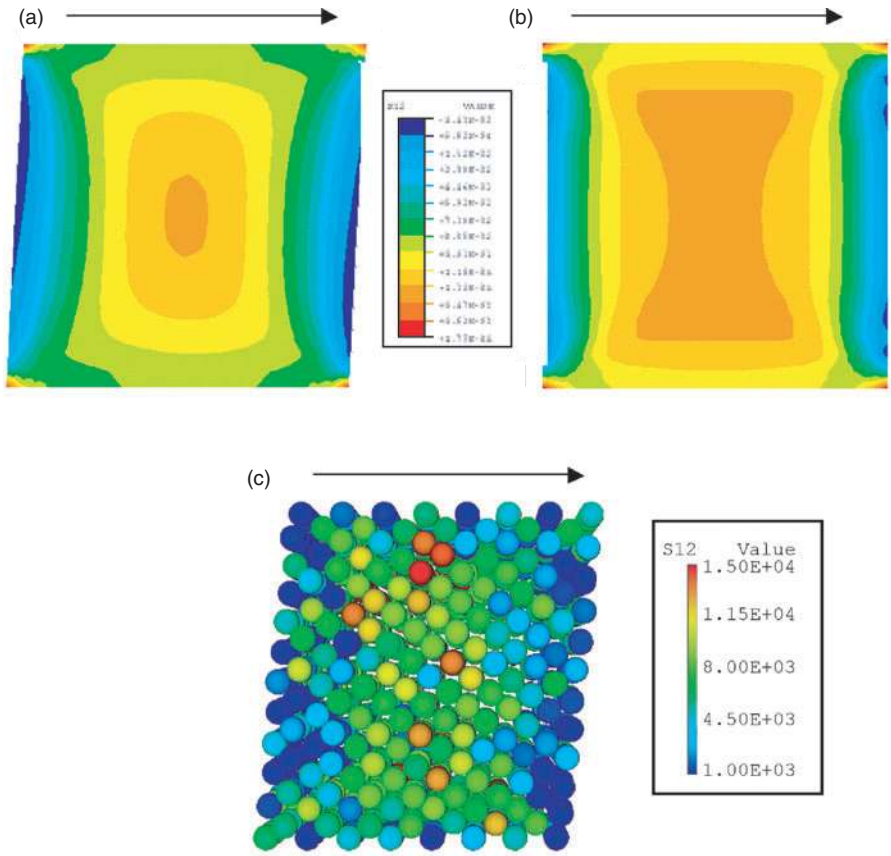

Figure 4. Shear stress contours (GPa) for a specimen with an aspect ratio of 1 : 1 at yield for (*a*) macroscale internal state variable theory (S12), (*b*) crystal plasticity (S12), and (*c*) atomistics (yellow are low shear stresses and brown are high shear stresses; arrows denote relative displacements).

the crystal plasticity simulation is qualitatively different than the macroscale ISV simulation due to the rate of change of the crystal orientation. Figure 7(*d*) shows that for one of the Euler angles with an initialization of 90° throughout the bulk at yield we see an angle decrease in some elements by 5° at the corners indicating that local rotations play a role in accommodating the simple shear boundary conditions. When you couple this information with the atomistic simulation results of dislocation nucleation, you can deduce that the gradient in rotation plays a role in the nucleation of dislocations.

Similar to figures 4–7 at 'apparent' yield, we show the simulation responses at 30% strain, which puts the simulations well into the plasticity region in figures 8–11. The stress and strain plots in figures 8–11 show similar trends as the yield plots. The similarities between the three different numerical methods is again very close when considering the kinematic responses and is qualitatively similar for the stress distributions. One interesting observation related to figure 11(*d*) is that the crystal orientation has changed from an initial orientation of 90° to almost 30° for some elements for the x/y aspect ratio of eight, indicating a very large difference in rotations for some elements of the crystal plasticity simulation.

Another similarity between the three computational methods can be seen in figure 12. Figure 12 shows the volume averaged yield stresses normalized by the shear modulus over

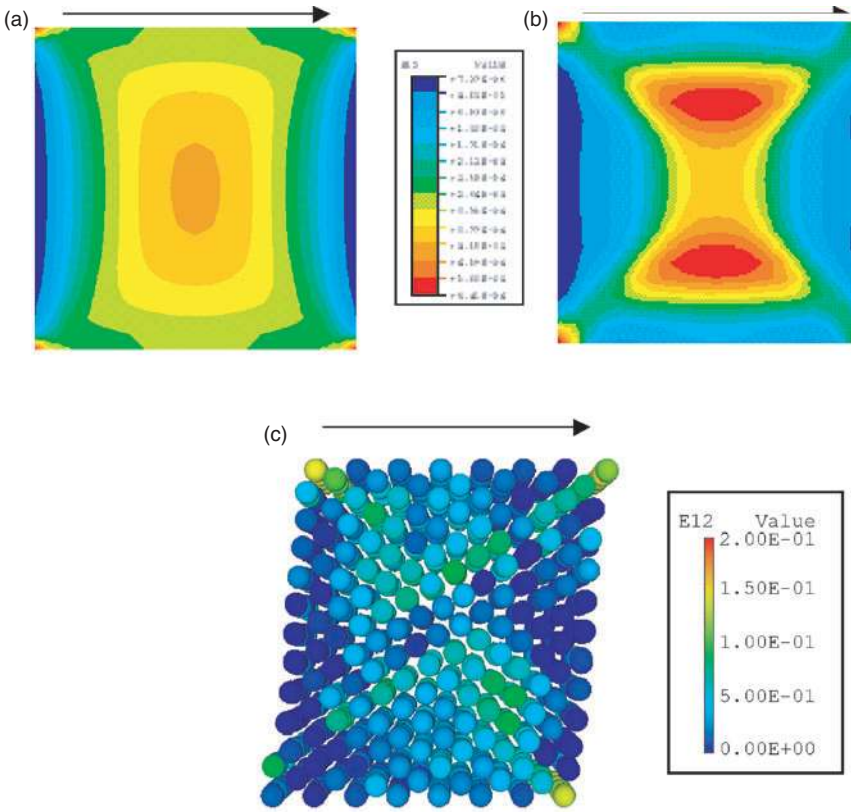

Figure 5. Shear strain contours for a specimen with an aspect ratio of 1 : 1 at yield for (*a*) macroscale internal state variable theory (E12), (*b*) crystal plasticity (E12), and (*c*) atomistics (yellow are low shear strains and brown are high shear strains; arrows denote relative displacements).

the specimen with varying aspect ratios for the macroscale internal state variable theory simulations, crystal plasticity simulations, and the atomistic simulations. This plot illustrates that as the x/y aspect ratio of the specimen increases, the yield stress increases until a saturation is achieved. Further, as the y/x aspect ratio of the specimen increases, the yield stress decreases. In figure 12(*a*), the yield stress increases as the x/y ratio increases until a saturation level is reached at an aspect ratio of approximately eight. Horstemeyer and Baskes (1999) proposed that this could arise for two reasons. Because the stress gradients near corners induced dislocations that determine the yield point, a more bulk-like response arises as the material in the x-direction is increased, then the global effect of dislocations nucleating from the corner decreases. Another notion to describe the x/y ratio increase in shear stress comes from an argument that image force effects could aid the nucleation event. However, the crystal plasticity and macroscale ISV theory show the same qualitative stress and strain gradients, and these numerical treatments do not include explicit functions for dislocation nucleation or image force effects.

Since we have discussed the qualitative similarities of the three computational methods, we now discuss their quantitative differences. In figures 4–11, at yield and at large strains, we saw similar trends in the kinematic and stress response. In figure 12, we saw that the specimen aspect ratio differences gave similar trends in the stress response. However, in each of the cases the stress magnitudes are different for the three different numerical methods.

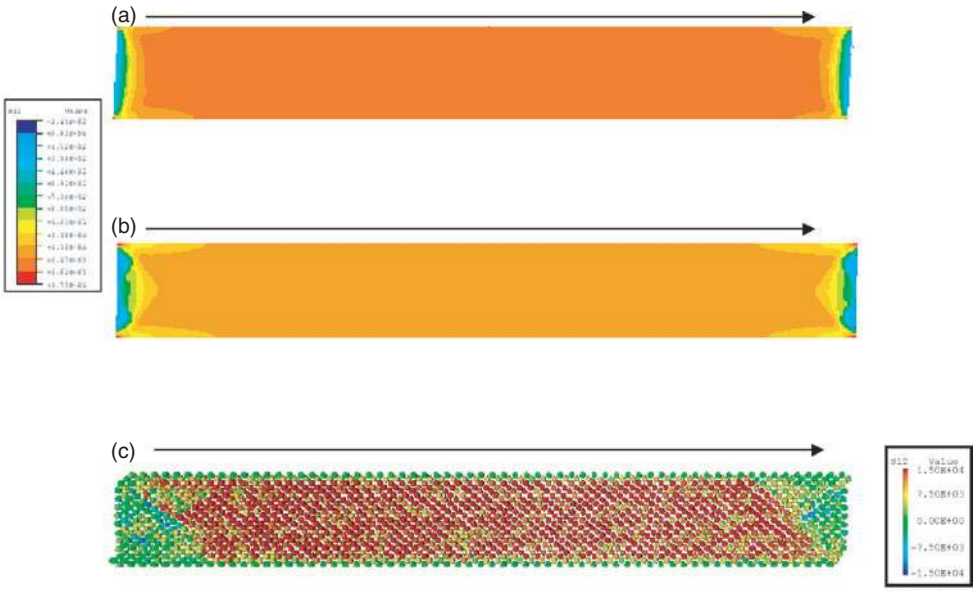

Figure 6. Shear stress contours (GPa) for a specimen with an aspect ratio of 8 : 1 at yield for (*a*) macroscale internal state variable theory (S12), (*b*) crystal plasticity (S12), and (*c*) atomistics (yellow are low shear stresses and brown are high shear stresses).

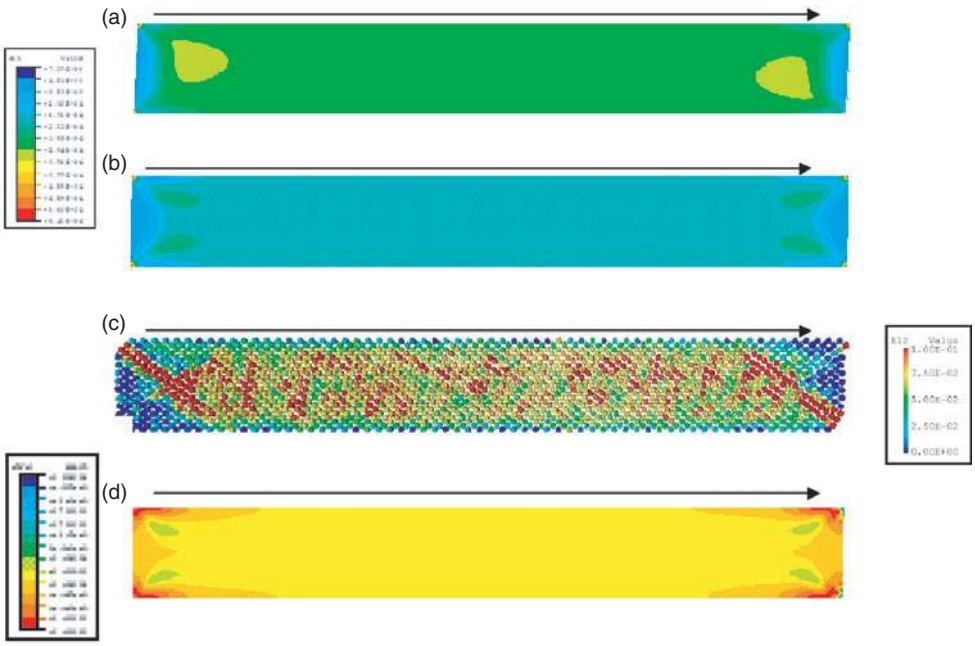

Figure 7. Shear strain contours for a specimen with an aspect ratio of 8 : 1 at yield for (*a*) macroscale internal state variable theory (E12), (*b*) crystal plasticity (E12), and (*c*) atomistics (yellow are low shear strains and brown are high shear strains). Orientation angle (SDV37) from the crystal plasticity simulation is given in (*d*).

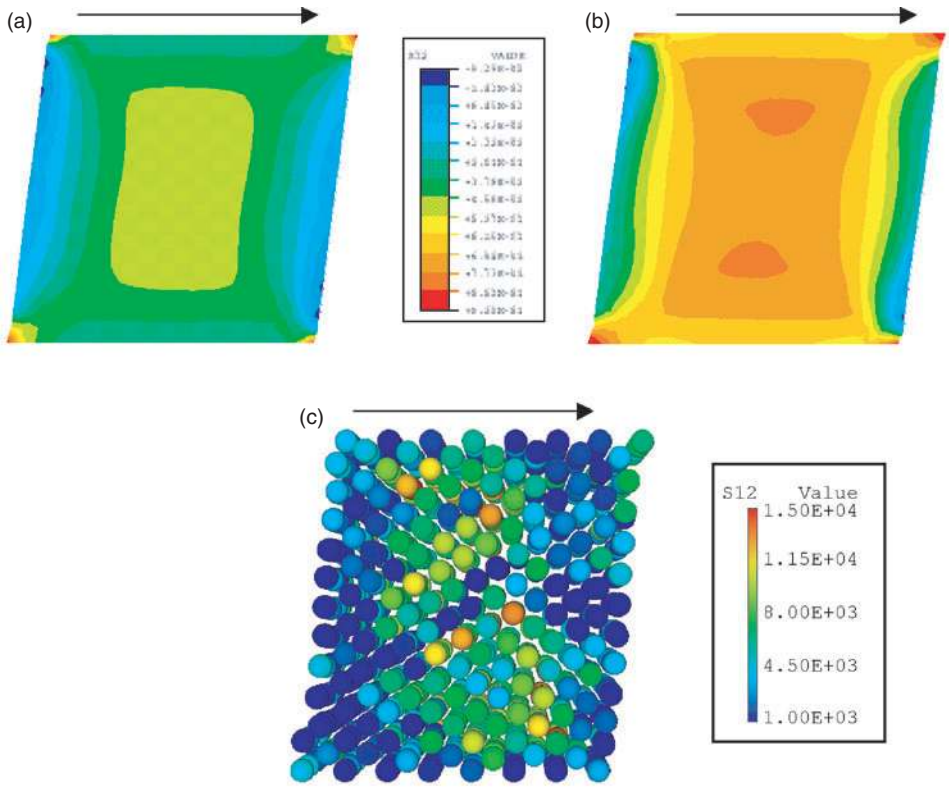

Figure 8. Shear stress contours (GPa) for a specimen with an aspect ratio of 1 : 1 at 15% strain for (*a*) macroscale internal state variable theory (S12), (*b*) crystal plasticity (S12), and (*c*) atomistics (yellow are low shear stresses and brown are high shear stresses; arrows denote relative displacements of atoms).

In figure 12 note that the ordinate has logarithmic units so as the size of the material decreases, the yield stress significantly increases. This occurs because the strength of a solid is inversely proportional to the material size as described by Horstemeyer and Baskes (1999). For the atomistic simulations, we conducted simulations with the same aspect ratios for the blocks of material but with different absolute sizes to illustrate the length scale effect. The macroscale ISV theory and crystal plasticity formulation do not have an inherent length scale included. However, with the crystal plasticity and macroscale ISV theory do show the general trend of size scale dependence as the material model parameters were determined from large scale single crystal data and polycrystalline data. This results because the ratio of homogeneous deformation to inhomogeneous deformation increases as the length-to-height ratio increases in all of the computational methods.

Now, we would like to discuss the contrasting results from the varying aspect ratios of the specimens. Using the macroscale ISV theory figure 13 illustrates that when the length-to-height (x/y) aspect ratio transitions from eight to unity, the stress distribution is *more* diffuse because of the influence of the gradients. When the x/y aspect ratio transitions from unity to eight, the stress distribution becomes *less* diffuse as shown in figure 13. One can think of large x/y ratios as 'pure' simple shear and small x/y ratios as 'pure' bending. When the ratio approaches unity, a combined multiaxial response results. Note that if the distribution

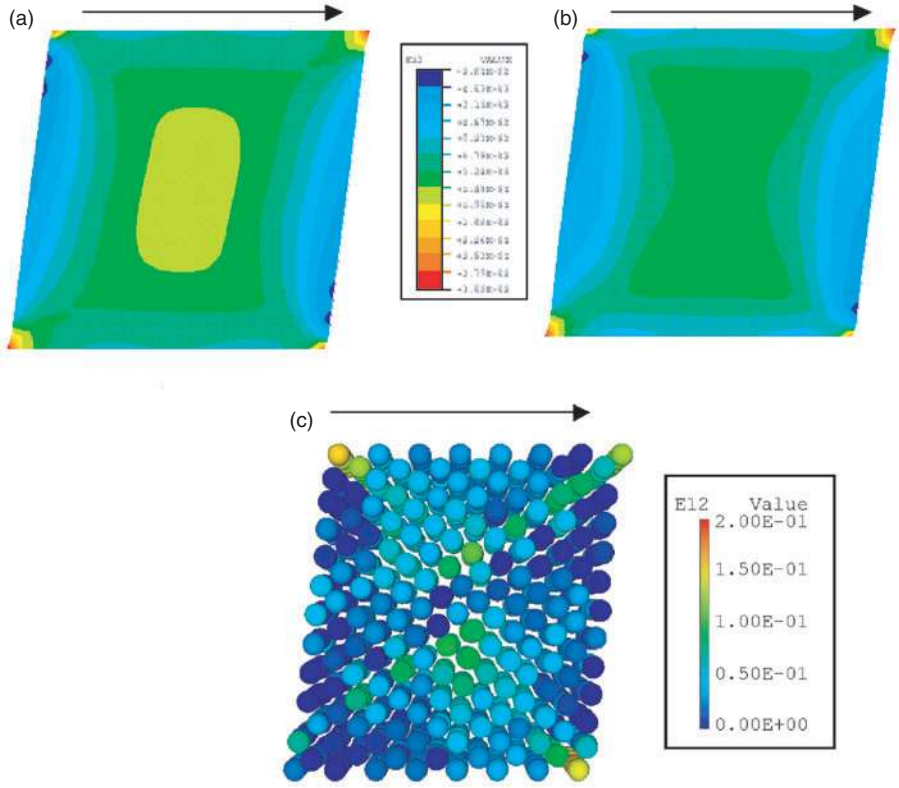

Figure 9. Shear strain contours for a specimen with an aspect ratio of 1 : 1 at 15% strain for (*a*) macroscale internal state variable theory (E12), (*b*) crystal plasticity (E12), and (*c*) atomistics (yellow are low shear strains and brown are high shear strains; arrows denote relative displacements of atoms).

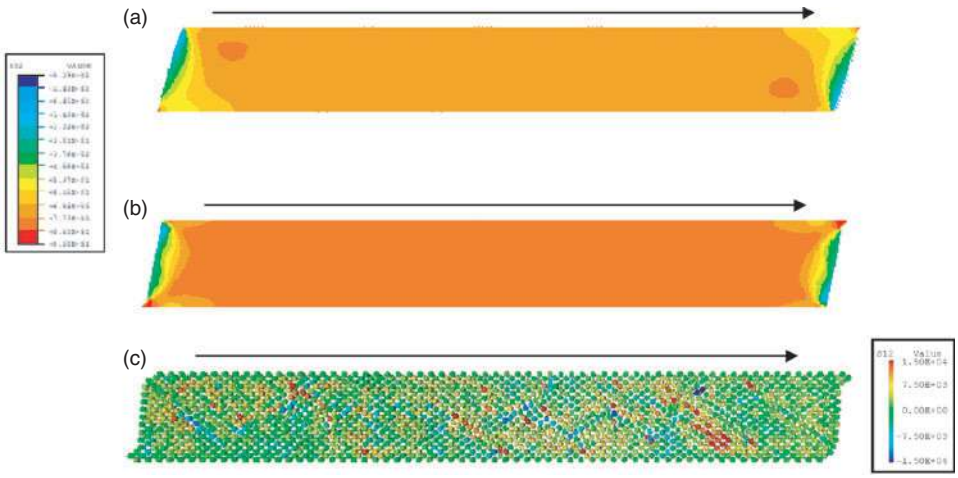

Figure 10. Shear stress contours (GPa) for a specimen with an aspect ratio of 8 : 1 at 30% strain for (*a*) macroscale internal state variable theory (S12), (*b*) crystal plasticity (S12), and (*c*) atomistics (yellow are low shear stresses and brown are high shear stresses; arrows denote relative displacements of atoms).

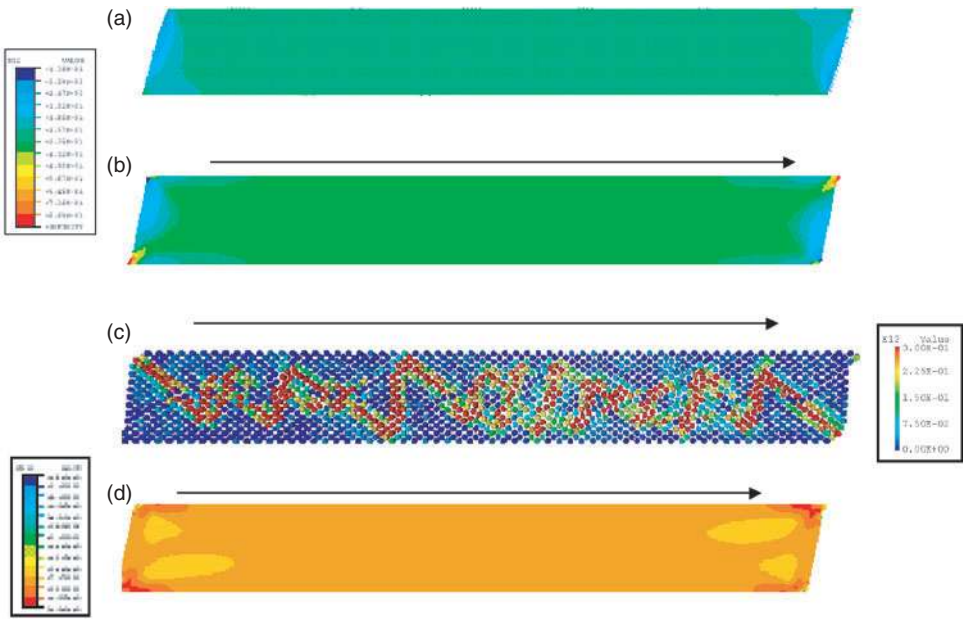

Figure 11. Shear strain contours for a specimen with an aspect ratio of 8 : 1 at 30% strain for (*a*) macroscale internal state variable theory (E12), (*b*) crystal plasticity (E12) and (*c*) atomistics (yellow are low shear strains and brown are high shear strains; arrows denote relative displacements of atoms). Crystal orientations (SDV37) are shown from the crystal plasticity simulation in (*d*).

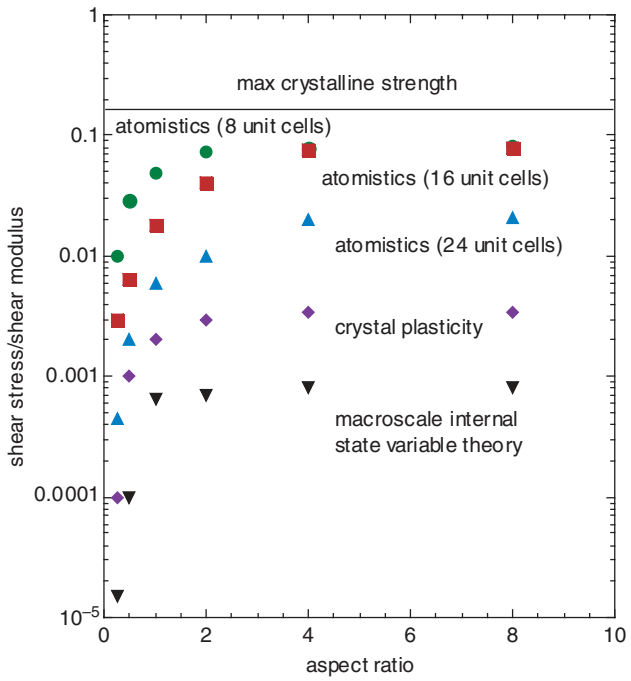

Figure 12. Average yield stress for a block of material of varying aspect ratios computed with different modelling methods.

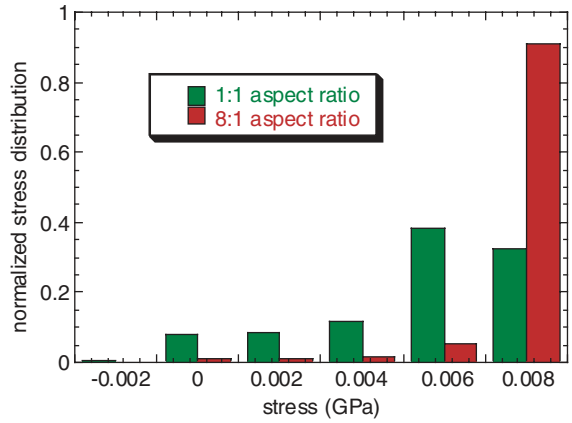

Figure 13. Stress distribution normalized by highest local stress from macroscale ISV model finite element analysis for different aspect ratios under simple shear.

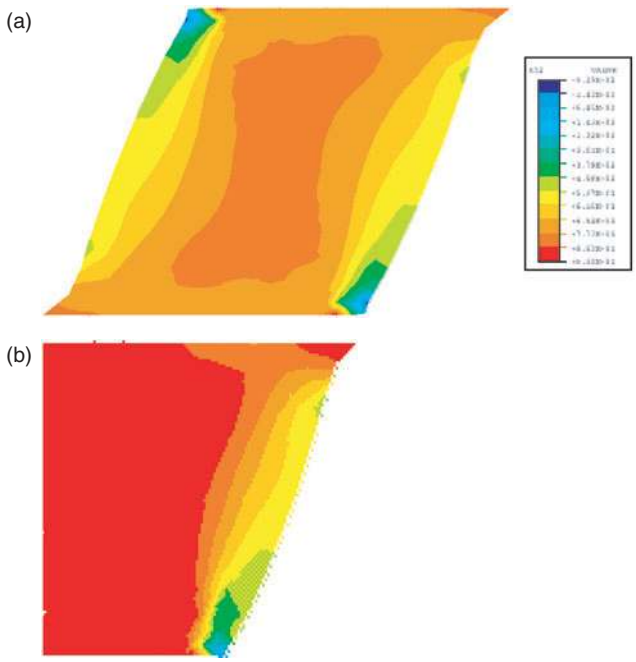

Figure 14. Shear stress contours (S12) of (*a*) 1 : 1 and (*b*) 8 : 1 specimens after 30% shear strain. Both blocks show similar distribution of stresses in corners despite different aspect ratios.

of stresses is volume averaged, like in the data in figure 12, as the x/y aspect ratio increases, the stress increases. This occurs even though a very similar stress distribution occurs in the corners of specimens for the x/y aspect ratios of unity and eight as shown from the ISV model simulation in figure 14 (which exaggerates the effect from the yield point because these stress contours are shown at 30% strain). However, when the x/y aspect ratio is near unity, the gradients in stress from the corners play more of role than the average values in the centre of the specimen. Essentially, the corners introduce inhomogeneous deformation,

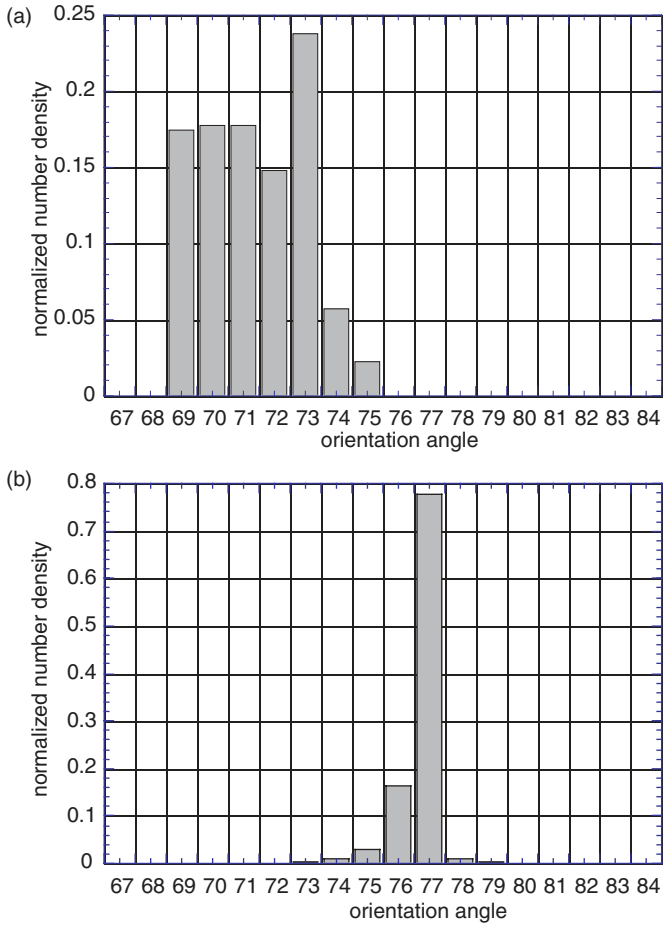

Figure 15. Comparison of orientation angle distribution at 30% strain from the (*a*) 1 : 1 and (*b*) 8 : 1 specimens from the crystal plasticity calculations.

but the centre of the specimen accommodates homogeneous deformation. As the aspect ratio size increases in either direction, the average stress swamps out the gradient effects. Based on these observations, we can conclude that the stress gradients drive the atomic level dislocation nucleation events as well.

From figure 12(*b*), one can see that as the y/x ratio increases, the yield stress decreases. Horstemeyer and Baskes (1999) claimed that volume per surface area of the specimen represents a length scale that correlates to yield and is illustrated by increasing the surface area on the y-face of the material block. Horstemeyer *et al* (2001a, b) also showed that this length scale dependence occurs at varying applied strain rates. With this in mind, we perform similar crystal plasticity and macroscale ISV simulations to gain some insights into the material responses. Essentially, as the height increases, the mechanism for inducing yield changes because the stress state changes from simple shear to one in which normal stresses are dramatically increased (more bending involved). As such, the volume averaged yield is lowered. Clearly, the response in figure 15 is different when compared to figure 2, which shows a specimen with a y/x ratio of 0.125. The larger y/x ratio appears to not only have

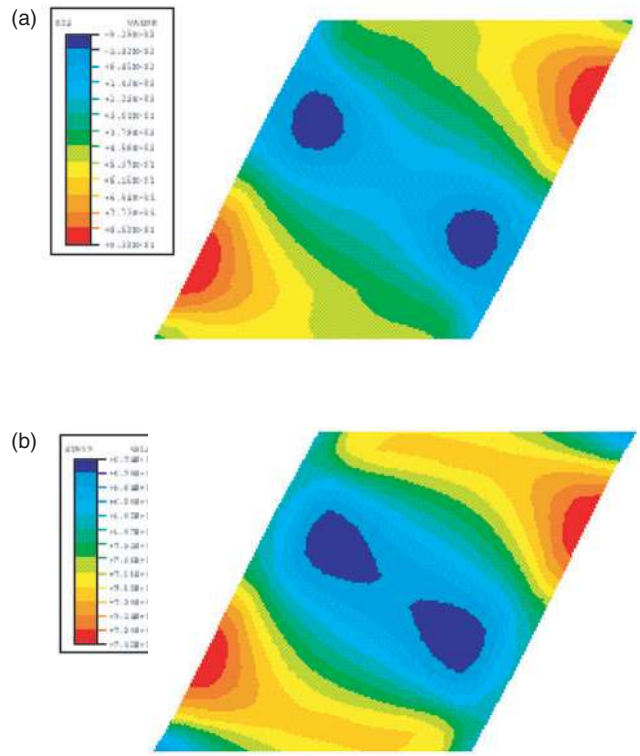

Figure 16. Colour contours of (*a*) shear stress (GPa) and (*b*) crystal orientation illustrating dependence of stress state on lattice orientation.

more surface area available for dislocation nucleation, but experiences material thinning and a inhomogeneous deformation from beam bending, where the smaller x/y ratio (or larger x/y ratio) shows a more 'homogeneous' deformation.

When a distribution of the angles is monitored and compared to the x/y aspect ratio of unity as shown in figure 15, we see that the x/y aspect ratio of eight has a less diffuse distribution of angles than the x/y aspect ratio of unity. The smaller x/y aspect ratio almost has an even distribution from 69° to 75°, but the larger x/y aspect ratio has a distribution that mostly saturates at 77°. Hence, the width and mean value of the distributions are different. This observation is consistent with those made for the stresses. In fact, the gradient in crystal rotation corresponds well with the gradients shown by the shear stresses and shear strains as illustrated in figure 16, which shows the x/y aspect ratio of unity at 30% strain.

Although these three different numerical methods show stress and strain gradients at the same locations within the specimen, the magnitude of the stress gradients are slightly different and can be illustrated when the results from the different simulations are normalized as shown in figure 17. The ordinate in figure 17 is the relative frequency of the local value for the shear stress divided by the total number of elements (for the FEM simulations) or number of atoms (for the EAM simulations). This helps to normalize the number density of the different simulations. The abscissa in figure 17 is the local shear stress (equation (3)) divided by the average global stress (equation (4)). The results in figure 17 show that the mean values are normalized at unity. The data to the right of the mean value illustrates the stress gradients that arise from the specimen corners with higher local shear stresses than average. The data to the

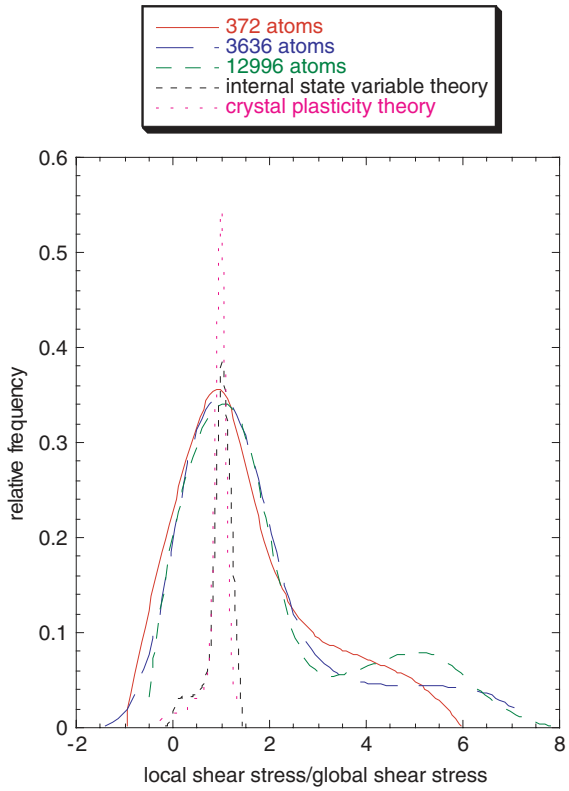

Figure 17. Relative frequency of local shear stress over the global average stress at yield for an aspect ratio of 2 : 1 for the internal state variable theory, crystal plasticity theory, and three different block sizes of atomistic simulations.

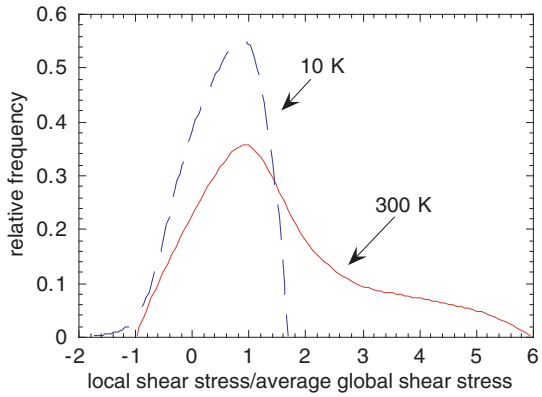

Figure 18. Relative frequency of local shear stress over the global average stress at yield for an aspect ratio of 2 : 1 for an atomistic simulation at 10 and 300 K for 372 atoms of nickel.

left of the mean value represent the atoms and elements on the left and right x-faces away from the corners. The stress and strain gradients that arise from the transition of the corner to the face occur where the dislocations nucleate in the atomistic simulations. Note from the atomistic simulations that as the size increases, the normalized distribution does not change. However,

the crystal plasticity and internal state variable results show a much narrower distribution than the atomistic simulations. Furthermore, the lower bump that is observed to the right of the mean value in the atomistic simulations is to the left in the finite element simulations. These two differences can be explained from a kinetics perspective. The 300 K atomistic simulations include fluctuations of local stresses from thermal vibrations. These vibrations do not exist in the finite element simulations. To illustrate this point, we ran the smallest block of atoms (372 atoms) at 10 K with the same boundary conditions. The results in figure 18 show that the 10 K simulation has a much narrower distribution and a lower bump to the left of the mean, much like the finite element simulations. In the 10 K simulation, the thermal vibrations are reduced to a minimum.

4. Conclusions

In this study, we compared and contrasted three different numerical methods representing three different size scales of simulations (atomistic modelling, crystal plasticity using finite elements, and internal state variable theory using finite elements). Qualitative similarities were found related to the yield stress of the specimens as a function of aspect ratio. As the x/y aspect ratio of the specimen increased (close to simple shear conditions), the yield stress increased until the ratio reached about 8 : 1 in which the yield stress saturated. Similarly, as the y/x aspect ratio of the specimen increased (close to bending conditions), the yield stress decreased until the ratio reached about 8 : 1 in which the yield stress saturated. The three different numerical methods also gave similar qualitative responses related to inhomogeneous stress and strain distributions in the corner regions of the specimens and a centralized homogeneous deformation region. However, several differences in the three numerical methods were evidenced. When comparing the distribution for the finite element analyses to the atomistic simulations, a much narrower stress distribution arose for the finite element analyses due to the lack of thermal vibrations experienced in the atomistic simulations. A 10 K atomistic simulation which dampened out the high frequency thermal vibrations verified this notion. A size scale effect related to the volume averaged shear stress in the specimen was evidenced. As the specimen size increased, the yield stress decreased. Finally, when comparing the three different numerical methods, the place of highest dislocation nucleation occurred where the highest plastic spin, highest stress gradients, and highest strain gradients occurred.

Acknowledgments

This work has been sponsored by the US Department of Energy, Sandia National Laboratories under contract DE-AC04-94AL85000.

References

Armstrong P J and Frederick C O 1966 *CEGB Report* RD/B/N, p 731
Asaro R J 1983 *J. Appl. Mech.* **50** 921
Bammann D J 1990 *Appl. Mech. Rev.* **1** 312
Bammann D J, Chiesa M L, Horstemeyer M F and Weingarten L I 1993 *Structural Crashworthiness and Failure* ed N Jones and T Weirzbicki (Elsevier Applied Science) p 1
Bammann D J, Chiesa M L and Johnson G C 1996 *The. App. Mech.* ed Tatsumi, Wannabe and Kambe (Elsevier) p 259
Coleman B D and Gurtin M E 1967 *J. Chem. Phys.* **47** 597
Cuitino A M and Ortiz M 1992 *Modelling Simul. Mater. Sci. Eng.* **1** 225
Daw M S and Baskes M I 1984 *Phys. Rev.* B **29** 6443
Daw M S, Foiles S M and Baskes M I 1993 Materials science reports *A Rev. J.* **9** 251

Edington J W 1969 *Phil. Mag.* **19** 41
Hibbitt, Karlsson and Sorensen, Inc., ABAQUS 5.8, 1998
Hill R and Rice J R 1972 *J. Mech. Phys. Solids* **20** 401
Horstemeyer M F and McDowell D L 1998 *Mech. Mater.* **27** 145
Horstemeyer M F and Baskes M I 1999 *J. Eng. Mater. Technol.* **121** 114
Horstemeyer M F, McDowell D L and McGinty R D 1999 *Modelling Simul. Mater. Sci. Eng.* **7** 253
Horstemeyer M F, Baskes M I and Plimpton S J 2001a *Acta Materialia* **49** 4363
Horstemeyer M F, Baskes M I and Plimpton S J 2001b *Theor. Appl. Fracture Mech.* **37** 49
Horstemeyer M F, Baskes M I, Hughes D A and Godfrey A 2002 *Int. J. Plasticity* **18** 203
Hughes D A and Nix W D *Met. Trans.* A **19** 3013
Hutchinson J W 1976 *Proc. R. Soc.* A **348** 101
Kelchner C, Plimpton S and Hamilton J 1998 *J. Phys. Rev.* B **58** 11085
Peirce D, Asaro R J and Needleman A 1982 *Acta Metall.* **30** 1087
Rice J R 1971 *J. Mech. Phys. Solids* **9** 433
Yoshida K, Goto Y and Yamamoto M 1966 *J. Phys. Soc. Japan* **21** 825